# Collisionless Shock Acceleration from Laser-Irradiated Foam Targets

**Contact:** benjamin.spiers@physics.ox.ac.uk

**B. T. Spiers, A. F. Savin**[a]**, R. Aboushelbaya, M. Mayr, R. W. Paddock, R. H. W. Wang, P. A. Norreys**
*Department of Physics,*
*University of Oxford,*
*OX1 3PU, United Kingdom*

**L. Ceurvorst, A. Casner**
*Centre Lasers Intenses et Applications (CELIA),*
*Université de Bordeaux-CNRS-CEA,*
*UMR 5107,*
*Talence F-33405, France*

**M. Fajardo**
*Department of Physics,*
*Instituto Superior Técnico,*
*Lisboa, Portugal*

[a]Now at Mewburn Ellis, LLP.

**C. D. Baird, M. Notley, C. Spindloe, S. Irving, R. Bingham**[b]
*Central Laser Facility,*
*Rutherford Appleton Laboratory,*
*OX11 0QX, United Kingdom*

**R. A. Cairns**
*University of St. Andrews,*
*Fife, Scotland*

**E. Boella**
*University of Lancaster,*
*Lancashire, England*

[b]Also at University of Strathclyde

## Abstract

An experiment was carried out at the Vulcan 100 TW laser facility to investigate the potential for collisionless shock acceleration in low-density plastic foam targets. To assist in interpretation of the spectra obtained, advances are made in the kinetic theory approach to collisionless shock theory first presented by Cairns *et al* in 2014. Experimental signatures consistent with acceleration from a collisionless shock were detected and parameter values which fit the form of the ion spectra are found. The parameter values found correspond to somewhat sub-optimal plasma conditions which arose due to experimental constraints.

## 1 Introduction

Acceleration of ions from laser-matter interactions has been the subject of much research, but well-understood mechanisms such as target-normal sheath acceleration (TNSA) produce broad, quasi-thermal ion spectra[1]. Two mechanisms for accelerating ions promise comparatively narrow-band ion spectra: radiation pressure acceleration, which has been achieved using $10\,\mu m$ $CO_2$ laser irradiation of correspondingly lower-density gas targets [2]; and collisionless shock acceleration (CSA), which was first realised in similar conditions (albeit with a significantly higher-intensity laser) by Haberberger *et al* [3], and has been achieved using $1\,\mu m$ pulses in gases by Chen *et al* and in laser-ablated foils by Pak *et al*, both at Lawrence Livermore Laboratory's Titan laser [4, 5]. Recently, Boella *et al* proposed the use of ions accelerated by a collisionless shock from the coronal plasma produced during an inertial confinement fusion (ICF) implosion to further heat the compressed fuel core to achieve fast ignition[6].

While Pak *et al* used a plasma ablated from a thin foil to produce plasma only a few times above critical density from a solid target, another possibility is the use of low-density solid foams, and it is this possibility which was investigated in the present work, at Vulcan's 100 TW Target Area West.

## 2 Experimental Setup

The approach taken in this experiment was to heat a CH plastic foam target using two of the Vulcan long pulse beams converted to the second harmonic.[1]

After two hundred picoseconds had passed allowing the plasma to homogenise (necessary given the highly inhomogeneous nature of solid foams) the resulting supercritical plasma was struck by a fundamental frequency pulse of 2 picosecond duration, carrying 70 joules of energy. This laser pulse set up the shock structure which then propagated through the plasma, accelerating protons and carbon ions.

Ions travelling parallel to the drive beam axis were captured and recorded by a Thomson spectrometer, allowing protons and carbon ions to be distinguished. Ion spectra were also recorded in the target-normal direction (which was rotated 10 degrees from the drive beam axis), to determine whether there was a significant difference in

---

[1]The long pulse beamlines were originally intended to be converted to the third harmonic, but this proved difficult to implement within the available time constraints.

the features of the spectrum due to the angular offset between the two axes. From prior work on TNSA[7] it was expected that some signal due to TNSA would be seen in the off-normal direction, albeit with fewer ions and a lower cut-off energy than in the target normal direction, but collisionless shock acceleration was only expected to produce a detectable ion signal in the drive laser normal direction.

## 3 Theory

The following derivation begins with a summary of the theoretical basis for a collisionless shock presented by Cairns *et al* [8, 9]. In Section 3.1, a systematic method for determining sets of parameters which can self-consistently describe a collisionless shock is presented for the first time. This method is inspired by, but significantly expands upon, the work presented by Savin [10]. The theory presented here is non-relativistic as this was deemed appropriate for the conditions used in this experiment, but a relativistic treatment has been presented by Stockem *et al* [11].

An electrostatic shock is characterised by an electric potential profile which rises from zero far upstream of the shock to a maximum value $\phi_{\max}$ at the shock front. This structure moves through plasma at a given shock speed, $V$, which is taken to be in the negative x direction (i.e. a velocity of $-V$). Ions whose velocity is $v_0 - V$ in the plasma rest frame have velocity $v_0$ in the rest frame of the shock, implying that the initial distribution of ion velocity in the shock frame, far upstream of the shock (where the electrostatic potential $\phi = 0$) is given by

$$f(v_0, \phi = 0) = n_0 \sqrt{\frac{m_i}{2\pi k_B T_i}} \exp\left(-\frac{m_i(v_0 - V)^2}{2k_B T_i}\right), \quad (1)$$

for an upstream ion population of mass $m_i$, temperature $T_i$ and uniform density $n_0$

From simple energy-conservation arguments, an ion of charge state $Z$ must have initial velocity greater than $v_{\min} = \sqrt{2Ze\phi/m_i}$ to reach a potential $\phi$. Having propagated up the shock to a potential $\phi < \phi_{\max}$, ions now have velocity $v = \sqrt{v_0^2 - v_{\min}^2}$. The steady-state form of the ion continuity equation leads to the condition $\frac{\partial}{\partial \phi}v(v_0, \phi)n_i(v_0, \phi) = 0$. Therefore the ion density at potential $\phi$, including ions with initial velocity of at most $v_{\max}$ is given by:

$$\tilde{n}_i(s, u_{\max}) \quad (2)$$
$$= b \int_{\sqrt{s}}^{u_{\max}} \frac{u}{\sqrt{u^2 - s}} \exp\left(-\beta_i\left(u - U\right)^2\right) du$$

In this equation the variables have been normalised for typographic brevity: number densities according to $\tilde{n}_i = n_i/n_0$, potentials according to $s = \phi/\phi_{\max}$,

and velocities according to $u^2 = m_i v^2/(2Ze\phi_{\max})$, and $b = (\beta_i/\pi)^{1/2}$ has been introduced for the sake of brevity. The ion temperature is represented as the normalised inverse temperature $\beta_i = Ze\phi_{\max}/(k_B T_i)$. An advantage of this normalisation of quantities is that it eliminates the maximum shock potential as an independent variable. This formulation differs from previous treatments which eliminate ion temperature and express integrals over the residual, not the initial velocity [8–10].

Electrons are parametrised by the electron temperature, which is normalised similarly to the ion temperature: $\beta_e = e\phi_{\max}/(k_B T_e)$. The temperature ratio emphasised by other treatments of this problem [8–10] is therefore given by $T = \beta_i/\beta_e$, and are distributed according to a Boltzmann relation:

$$\tilde{n}_e(s, u_{\max}) = Zn_i(0, u_{\max}) \exp(s\beta_e) \quad (3)$$
$$= Zb \exp(s\beta_e) \int_0^{u_{\max}} \exp\left(-\beta_i\left(u - U\right)^2\right) du$$

At a given $\phi$, two components contribute to the particle distributions: one component represents inflowing ions, for which $u_{\max} = \infty$; the other contains ions which have reflected from the shock and are travelling back upstream, whose $u_{\max} = 1$ such that all ions in this component have insufficient energy to pass through the shock. Therefore the total charge density at potential $\phi$ (normalised to $Zen_0$) is:

$$\rho(s) = (\tilde{n}_i(s, \infty) + \tilde{n}_i(s, 1))$$
$$- \frac{1}{Z}\left(\tilde{n}_e(s, \infty) + \tilde{n}_e(s, 1)\right). \quad (4)$$

The Sagdeev potential $\Phi$ (normalised to $\phi_{\max}$) is defined by

$$\frac{\partial^2 s}{\partial x^2} = -\frac{\partial \Phi}{\partial s}, \quad (5)$$

an equation identical in form to that of a particle moving under the influence of a potential $\Phi$, whose 'time' variable is $x$ and whose 'space' variable is $s$. Here $x$ is normalised to $v_\phi/\Omega_i$, where $v_\phi^2 = Ze\phi_{\max}/m_i$ and $\Omega_i$ is the standard ion plasma frequency.

Converted to an integral equation and employing the electrostatic Poisson equation with appropriate normalisation, the Sagdeev potential takes the form

$$\Phi(s) = \int_0^s \rho(s')\, ds'. \quad (6)$$

By comparison with Eq. 4, the Sagdeev potential is therefore a combination of four terms, each of which is a double integral. By considering that the 'pseudo-particle' moving according to Eq. 5 starts at $s = 0$, and that by inspection of Eq. 6 the Sagdeev potential $\Phi(0) = 0$, we can deduce that the highest value of $s$ that

the system evolving according to Eq. 5 will reach—by definition $\phi_{\max}/\phi_{\max} = 1$—also fulfils $\Phi(s) = 0$. Therefore the condition $\Phi(1) = 0$ closes the system and ensures self-consistent dynamics.

A necessary condition to ensure that the Sagdeev potential takes the form of a potential well, so that the pseudo-particle is able to reach $s = 1$, is

$$\left.\frac{\partial \Phi}{\partial s}\right|_{s=1} > 0. \qquad (7)$$

It remains to find sets of parameters $(U, \beta_i, \beta_e)$ for which $\Phi(s = 1) = 0$.

### 3.1 The Valid Parameter Space

Firstly we observe that in Eq. 3, $\tilde{n}_e$ is trivially integrable with respect to $s$:

$$N_e = \int_0^1 \tilde{n}_e(s, u_{\max})/Z \, \mathrm{d}s \qquad (8)$$
$$= \frac{\exp(\beta_e) - 1}{\beta_e} \tilde{n}_i(0, u_{\max}).$$

Integrating out the $s$-dependence in Eq. 2 is somewhat more involved, but the integrals involved are not difficult. By splitting the domain of the velocity integral at $u = 1$, inverting the order of integration to integrate first over $s$ and then comparing the resulting integrand in the two regions of the velocity integral, it can be shown that the result is

$$N_i = \int_0^1 \tilde{n}_i(s, u_{\max}) \, \mathrm{d}s \qquad (9)$$
$$= b \int_0^{u_{\max}} 2u \left(u - \Re\sqrt{u^2 - 1}\right) \qquad (10)$$
$$\exp\left(-\beta_i \left(u - U\right)^2\right) \mathrm{d}u$$

At this point it is informative to re-normalise velocities relative to the maximum velocity of reflected particles. Introducing $u = v_0/\sqrt{2\phi_{\max}}$ and $U = V/\sqrt{2\phi_{\max}}$ and also replacing the electron-ion temperature ratio $T$ with $\beta = \phi_{\max}/T$,

$$N_i = b \int_0^{u_{\max}} 2u \left(u - \Re\sqrt{u^2 - 1}\right) \qquad (11)$$
$$\exp\left(-\beta_i \left(u - U\right)^2\right) \mathrm{d}u$$
$$= F_{U,\beta_i}(u_{\max}) \qquad (12)$$
$$N_e = \frac{e^{\beta_e} - 1}{\beta_e} b \int_0^{u_{\max}} \qquad (13)$$
$$\exp\left(-\beta_i \left(u - U\right)^2\right) \mathrm{d}u$$
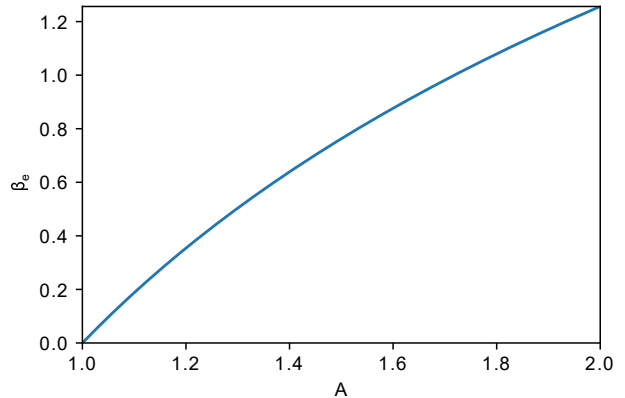$$= \frac{e^{\beta_e} - 1}{\beta_e} G_{U,\beta_i}(u_{\max}) \qquad (14)$$



Figure 1: The relationship between $\beta_e$ and $A$, the ratio of integrals defined in Eq. 16. It is clear that the constraints $\beta_e > 0$ and $A \leq 2$ correspond to $A \geq 1$ and $\beta_e \lessapprox 1.25$.

Now, the Sagdeev self-consistency condition is given by

$$0 = (N_i(\infty) + N_i(1)) \qquad (15)$$
$$- (N_e(\infty) + N_e(1)).$$

Rearranging to isolate $\beta_e$ on one side of the equation,

$$\frac{e^{\beta_e} - 1}{\beta_e} = \frac{F_{U,\beta_i}(\infty) + F_{U,\beta_i}(1)}{G_{U,\beta_i}(\infty) + G_{U,\beta_i}(1)} = A \qquad (16)$$

This equation can be solved for $\beta_e$ for given values of $U$ and $\beta_i$ to determine the electron temperature. Due to the simplified nature of the integrals involved, only $F_{U,\beta_i}(\infty)$ is not soluble analytically[2], and even that integral is sufficiently 'nice' to be evaluated numerically to relatively high accuracy[3].

Note that the condition $A > 1$ ensures that $\beta_e \geq 0$. The largest value $A$ may be expected to take is roughly two—the maximum value of $2u(u^2 - \sqrt{u^2 - 1})$—corresponding to a maximum $\beta_e = 1.25643$. The function $\frac{e^\beta_e - 1}{\beta_e}$, shown in Figure 1 has no inverse in terms of elementary functions, though a closed-form inverse exists and depends on the product logarithm special function. Given the small range of values taken by $A$, an interpolation approach to inverting $A(\beta)$ could also give acceptable accuracy.

### 3.2 The Cold-Ion Limit

We now examine the behaviour of the system for $\beta_i \gg 1$, corresponding to an ion temperature much smaller than the shock potential. For sufficiently large values of $\beta_i$, Equations 12 and 14 become

---

[2] $F_{U,\beta_i}(1)$ may be evaluated by noting that $\Re\sqrt{u^2 - 1} = 0$ where $0 \leq u \leq 1$.

[3] This integral takes the form of a convolution with a Gaussian kernel, a fact which could have potential for numerical evaluation, though this potential is not investigated here.
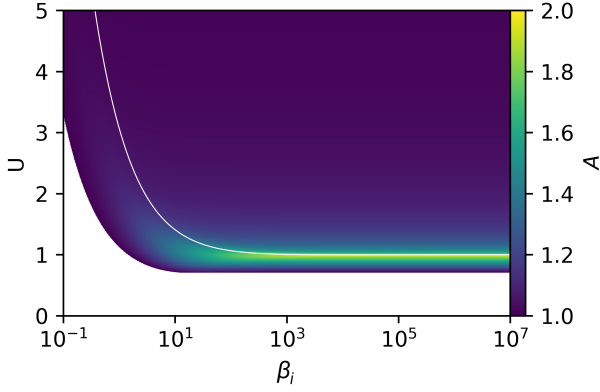
Figure 2: Values of the integral ratio $A$ for a range of values of the independent variables $U$ and $\beta_i$. Behaviour converges to a constant function $A(U)$ for large $\beta_i$ in agreement with Eq. 19. The space is divided into two regions by an overlaid white line corresponding to the locus $\frac{\partial \Phi}{\partial s}(s=1) = 0$. Above the line the condition of Eq. 7 is fulfilled, below it the gradient is negative and no shock forms. This condition restricts the valid phase-space to $U \geq 1$

$$F(u_{\max}) = \begin{cases} 2U\left(U - \Re\sqrt{U^2 - 1}\right) & U < u_{\max} \\ 0 & U > u_{\max} \end{cases} \quad (17)$$

$$G(u_{\max}) = \begin{cases} 1 & U < u_{\max} \\ 0 & U > u_{\max} \end{cases} \quad (18)$$

This gives a value for $A$ in closed form:

$$\frac{e^{\beta_e} - 1}{\beta_e} = A = 2U\left(U - \Re\sqrt{U^2 - 1}\right) \quad (19)$$

For positive $\beta_e$, A must be larger than unity. This restricts the parameter space to $U^2 > \frac{1}{2}$. The minimum value of $U^2$ is further restricted by considering the condition of Eq. 7. Careful analysis shows that for $\phi_{\max} \gg 1$, this condition reduces to $U \geq 1$. For finite $\beta_i$ this condition has been numerically evaluated and the result is shown in Figure 2 as a line separating the region of space where this condition is fulfilled from that in which it is not. For all values of $\beta_i$, Eq. 7 is only fulfilled for $U \gtrapprox 1$. As $u = 1$ corresponds to the velocity required for an ion to pass the shock, this condition implies that only ions already moving towards the shock in the plasma rest frame can be reflected and therefore at most half of the plasma ions may be reflected by the shock.

As seen in Figure 2, or by inspecting Eq. 19, the maximum value attained by A is two, at $U = 1$. For $A = 2$, $\beta_e \approx 1.25643$. From these constraints we derive the following constraints on the parameter space in which CSA is possible, in physical units

$$Ze\phi_{\max} < \frac{1}{2}m_i V^2 \quad (20)$$

$$e\phi_{\max} < 1.25643 k_B T_e \quad (21)$$

The maximum of $e\phi_{\max}/k_B T_e$ is attained at $Ze\phi_{\max} = \frac{1}{2}m_i V^2$.

The admissible phase-space of the system is shown in Figure 3, in both $\beta - M$ space and for the purposes of comparison to previous work such as Savin [10] also in $T - M$ space, for which the space is not bounded as it is in $\beta - M$ space.

### 3.3 Ion Spectra

With the ability to find valid regions of $U - \beta_i - T$ phase-space, it is now desirable to find the energy spectrum of ions accelerated by a shock with these parameters. Dividing ions into three populations based on their initial velocity in the shock frame, it is possible to evaluate the velocities they are accelerated to, and therefore their energies in the lab frame. Ions with initial velocity $u < 0$, i.e. those travelling downstream of the shock, are not affected by the potential of the shock and so their velocity is unchanged by the shock. Ions with initial velocity $0 < u < 1$ reflect from the shock, and their final velocity is negated in the shock frame. Those with initial velocity $u > 1$ pass through the shock without being reflected – their velocity is reduced to $\sqrt{u^2 - 1}$ in the shock frame. Transforming these velocities into the lab frame, and negating the sign of velocities such that reflected ions have positive velocity:

$$u_{\text{lab}} = \begin{cases} u_{\text{E}} - u_{\text{rf}} & 0 > u_{\text{rf}} + U \\ u_{\text{E}} + 2U + u_{\text{rf}} & 0 < u_{\text{rf}} + U < 1 \\ u_{\text{E}} + U - \sqrt{(u_{\text{rf}} + U)^2 - 1} & 1 < u_{\text{rf}} + U \end{cases} \quad (22)$$

for ions with initial velocity $u_{\text{rf}}$ in the plasma rest frame, which is itself moving with the expansion velocity $u_E$ relative to the lab frame.

Transforming these into normalised energies, $E = u_{\text{lab}}^2$:

$$f_{\text{E}}(E) = \begin{cases} f_u(u_{\text{back}}(E))\frac{\partial}{\partial E}u_{\text{back}} & U_{\text{E}}^2 < E \\ f_u(u_{\text{slow}}(E))\frac{\partial}{\partial E}u_{\text{slow}} & U_{\text{E}}^2 < E < (1 + U_{\text{E}})^2 \\ f_u(u_{\text{fast}}(E))\frac{\partial}{\partial E}u_{\text{fast}} & 0 < E < U_{\text{E}}^2 \end{cases} \quad (23)$$

where the lab-frame shock speed $U_{\text{E}} = U + u_{\text{E}}$ has been introduced

Here values of $f_{\text{E}}(E)$ in regions where two of the three conditions overlap are calculated by adding together values for the applicable regions, $f_u(u) \propto \exp\left(-\beta_i u^2\right)$ and
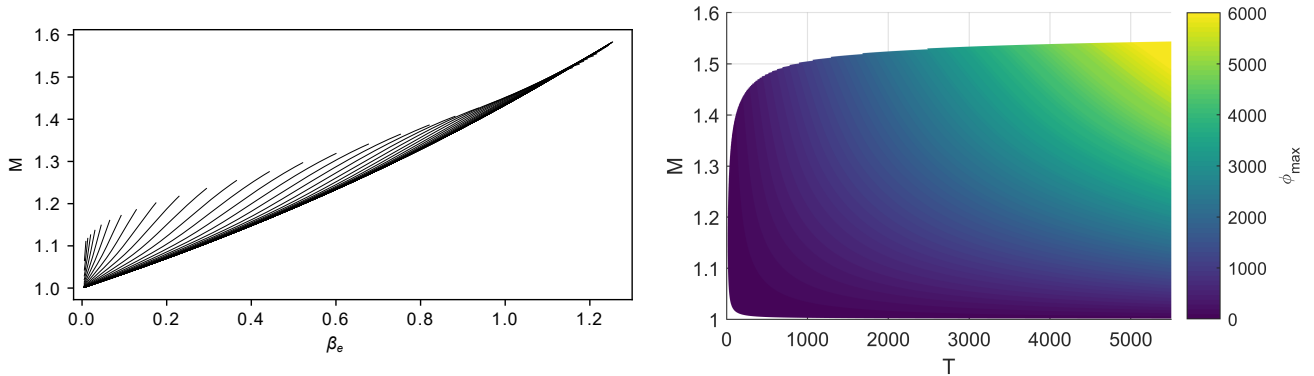
4

Figure 3: The valid phase space of the collisionless shock system, (left) represented by lines of constant $\beta_i$ in $\beta_e - M$ space and (right) in $T - M$ space. The space is fully bounded in $\beta_e$ and $M$, but unbounded in $T$ and $\phi_{\max} = \beta_i$. In the left pane, large values of $\beta_i$ tend to the lower limiting line and small values of $\beta_i$ tend toward the $\beta_e = 0$ limit at the left.

the functions:

$$u_{\mathrm{back}}(E) = u_{\mathrm{E}} - \sqrt{E} \qquad (24)$$

$$u_{\mathrm{slow}}(E) = \sqrt{E} - u_{\mathrm{E}} - 2U \qquad (25)$$

$$u_{\mathrm{fast}}(E) = \sqrt{(u_{\mathrm{E}} + U - \sqrt{E})^2 + 1} - U \qquad (26)$$

give the initial plasma-frame velocity in terms of the lab-frame energy. Figure 4 presents an example spectrum for parameters $U = 1.01$, $\beta_i = 1000$. The high-energy cut-offs for these two populations are in the ratio $(U+1)^2/U^2$, so it is in principle possible to determine the normalised shock-speed $U$ from the form of an ion spectrum alone. In practice however, as seen in Section 4 and in particular Figure 5, these lowest-energy ions may be lost due to the working range of ion spectrometers not reaching down to zero energy, or obscured by ions accelerated by other mechanisms such as TNSA.
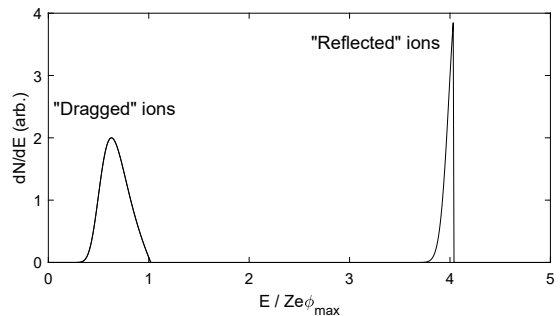
## 4  Results

Ion spectra collected from the drive beam using a Thomson spectrometer on two different shots are shown in Figure 5. Thermal (i.e. with $N \approx \exp(-E/kT)$ dependence) proton populations are clearly visible, with similar temperature shared by the protons captured along each shot. The energy dependence of these beams is consistent with target-normal sheath acceleration. TNSA appears to be suppressed at energies above approximately $1.25\,\mathrm{MeV}$[4]. A narrower peak ranging from $1.5\,\mathrm{MeV}$ to $1.75\,\mathrm{MeV}$ is compared to the spectrum predicted by the model of Section 3.3 with dimensionless parameters $\beta_i = 10$, $U = 1.45$ and ion temperature $k_B T_i = 28\,\mathrm{keV}$. No such narrow peak was ever observed in the target-normal direction.



Figure 4: Ion spectrum predicted by the model of Section 3.3 for parameter values $U = 1.01$, $\beta_i = 1000$. Note the population of approximately thermal ions with cut-off energy approximately equal to the shock potential energy which have been "dragged" by the shock, and the narrow, sharp population of ions reflected from the shock with energy approximately four times the shock potential. Note the energy axis is normalised according to the physical ion potential energy $Ze\phi_{\max} = \beta_i k_B T_i$.
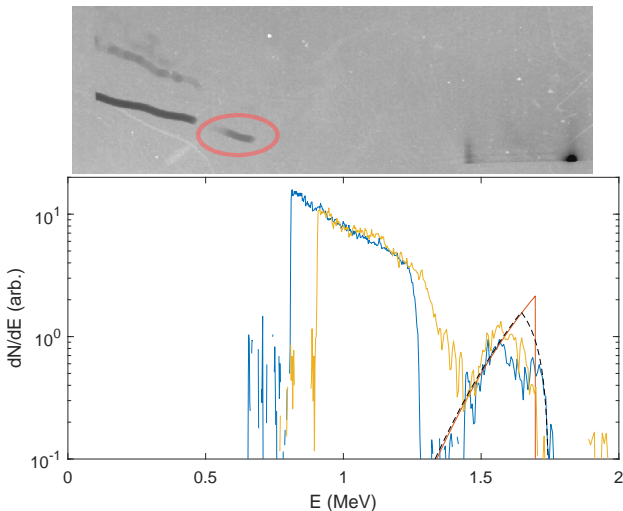
---

[4]Ions with energy below about $0.75\,\mathrm{MeV}$ are lost from the detector, explaining the sharp low-energy cut-off

The analysis of Section 3 predicts electron-ion temperature ratio $T = 27$ and therefore Mach number $M = 1.24$ for the parameters noted above. In physical units $\phi_{\max} = 284\,\mathrm{kV}$, $k_B T_e = 769\,\mathrm{keV}$, $V = 3.6\%$ of $c = 10\,\mathrm{\mu m\,ps^{-1}}$. While the overall width of the spectra are comparable, the prediction is much more strongly peaked, with a sharp maximum energy cut-off. The loss of this sharp definition in the experimental spectrum may be due to the use of a large pinhole, the shape of which is colvolved with the true spectrum and therefore broadens sharp features. The effect of such a convolution is also shown in Figure 5.

### 4.1 Uncertainty in Derived Parameters

The three parameters mentioned above—the normalised inverse ion temperature $\beta_i$, normalised shock speed $U$ and physical ion temperature $k_B T_i$—are sufficient to fully determine the behaviour of the collisionless shock system, including the physical electron temperature via its dimensionless inverse $\beta_e$, and the Mach number $M$ used to characterise the shock speed. While values of these three parameters have been found in the above paragraphs which reproduce the form of the spectrum found in the experiment, it is important to qualify this by examining how much the parameters can vary and produce similarly-shaped spectra. In the following analysis the peak of the reflected spectrum is normalised to a constant value. This is because absolutely calibrated comparison of the number of ions accelerated to theoretical predictions would require very detailed accounting of the ion density and size of the target, the angular spread of the beam and the pinhole at the entrance to the spectrometer, as well as an absolutely calibrated detector. The former is beyond the scope of this report, and no absolute calibration of the image plates used to collect spectra was carried out during the experiment.

The maximum energy cut-off of the reflected ion spectrum is easy to determine both theoretically and by inspection of the spectra: following Section 3.3, the maximum energy in physical units is $E_{\max} = (1+U)^2 \beta_i k_B T_i$. Once the maximum energy has been read off an ion spectrum, this forms a constraint between the three key parameters – if a shock speed parameter $U$ and ion temperature $k_B T_i$ are chosen the normalised potential may be calculated easily. As a simple heuristic to link the two remaining parameters, the half-maximum point of the reflected spectrum is chosen to remain fixed. By differentiating the functional form of the reflected spectrum given in Section 3.3 with respect to $k_B T_i$ and setting the result to zero (evaluated at the half-maximum energy of the spectrum), a condition linking $U$ and $k_B T_i$ is found. Figure 6 shows an ensemble of normalised spectra generated by varying $U$ between 1.2 and 5[5] and using these



Figure 5: Top: A reading from a Thomson parabola spectrometer featuring the characteristic isolated region of proton flux (circled in red) attributed to collisionless shock acceleration. Bottom: (blue) proton spectrum extracted from the above image plate data and (yellow) another representative shot displaying a CSA-like peak. Red: The prediction of Section 3.3 for dimensionless parameter values of $\beta_i = 10$, $U = 1.45$. We do not attempt to fit to the regions of exponential energy dependence with $E < 1.25\,\mathrm{MeV}$ as these protons are assumed to be accelerated by a TNSA-like mechanism, not CSA. The dashed black line demonstrates the effect of finite pinhole size on the apparent energy distribution.

---

[5]Here the lower limit is enforced by the condition of Equation 7 and the upper limit determined by considering the maximum energy of non-reflected ions.

two constraints to calculate the corresponding values of the other parameters. Note that the ensemble shown in Figure 6 is only a one-dimensional traversal through parameter space – a more rigorous uncertainty analysis may be able to expand this to a two-dimensional region of the phase space all corresponding to similar spectral traces, but this is left for future work. Even without this more detailed analysis further expanding the parameter space which produces equivalent spectra it is clear that there is much uncertainty present in the determination of experimental parameters from the ion spectrum alone. This is exacerbated by the failure of an x-ray spectrometer deployed on the experiment to produce usable data, preventing assessment of the electron temperature of the plasma.

Numerical radiation-hydrodynamic simulations were carried out to try to determine the initial conditions of the plasma prior to short-pulse irradiation, but these simulations did not produce results consistent with even the broad range of parameters which produce the observed ion spectra. However, variables such as temperature are expected to depend strongly on the equation of state of the foam target. Equations of state of foams are poorly-understood and will not necessarily agree with the equations of state for homogeneous materials, which were simply used at much lower than solid density to facilitate these simulations. This discrepancy between the physical and assumed equation of state may explain the difficulty in modelling the targets for this particular experiment.

## 5 Conclusion

An experiment investigating the acceleration of proton beams by collisionless shocks has been carried out at the Vulcan 100 TW laser facility, using novel low-density solid foam targets to achieve the marginally over-critical plasma density required to produce the electrostatic shock structure. A population of quasi-monoenergetic protons was detected parallel to the drive beam axis, as well as a population matching the exponential energy dependence expected of target-normal sheath acceleration. The quasi-monoenergetic proton population detected in the drive beam direction is consistent with acceleration by a collisionless shock. The maximum energy cut-off and the breadth of this spectral signature are consistent with a large range of ion and electron temperature, shock speed and shock potential values, albeit within a constrained region of the full three-dimensional parameter space, shown in Figures 6 and 8. The maximum energy of ions accelerated is somewhat reduced compared to the prediction of Savin [10] for the Vulcan system. This prediction is shown in Figure 8 along with predictions for other systems. This may be understood by considering a number of factors by which the present experiment deviated from the idealised situation considered therein. Principal among them was the use of second-

harmonic irradiation to pre-form a plasma rather than third-harmonic, as originally proposed. The correspondingly enhanced opacity of the foam target to the heating beams—exacerbated by use of targets with higher-than-optimal density—prevented uniform heating of the target, and this non-uniformity was detrimental to the formation of a uniform, laminar shock.

Numerical modelling of the interaction was limited by the unavailability of necessary equation of state data for CH plastic initially in foam form, and resolving uncertainties in the key model parameters was therefore not possible using simulation results. Future experiments could provide more constrained estimates of the parameter values by making independent electron temperature measurements, and by measuring the electron density of the plasma, which may require development of a fourth-harmonic probe beam due to the high densities present. These measurements would provide a better understanding of collisionless shock formation within the plasma and enable optimisation of conditions to access the parameters range envisioned by Savin [10] at the Vulcan facility. Alternatively, facilities such as Orion or OMEGA, which regularly operate long pulses at third-harmonic and possess electron temperature and density diagnostics capable of probing denser plasma[12, 13], may be an appropriate setting for experiments of this type.

## References

[1] Daido, H., Nishiuchi, M. & Pirozhkov, A. S. Review of laser-driven ion sources and their applications. *Reports on Progress in Physics* **75**, 056401 (2012).

[2] Palmer, C. A. J. *et al.* Monoenergetic Proton Beams Accelerated by a Radiation Pressure Driven Shock. *Physical Review Letters* **106**, 014801 (2011).

[3] Haberberger, D. *et al.* Collisionless shocks in laser-produced plasma generate monoenergetic high-energy proton beams. *Nature Physics* **8**, 95–99 (2012).

[4] Chen, S. N. *et al.* Collimated protons accelerated from an overdense gas jet irradiated by a 1 μm wavelength high-intensity short-pulse laser. *Scientific Reports* **7**, 13505 (2017). URL https://www.nature.com/articles/s41598-017-12910-6. Number: 1 Publisher: Nature Publishing Group.

[5] Pak, A. *et al.* Collisionless shock acceleration of narrow energy spread ion beams from mixed species plasmas using 1 $\mu$m lasers. *Physical Review Accelerators and Beams* **21**, 103401 (2018).

[6] Boella, E. *et al.* Collisionless shock acceleration in the corona of an inertial confinement fusion pellet with possible application to ion fast ignition **379**, 20200039 (2020). URL
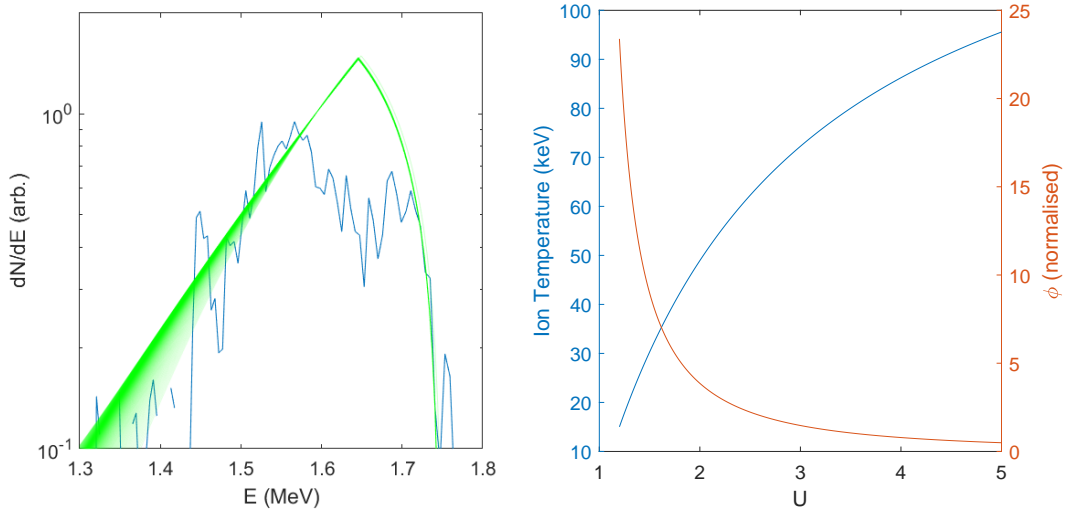
Figure 6: a) One of the spectra shown in Figure 5, overlaid with an ensemble of spectra calculated using the model of Section 3.3. The parameter $U$ is varied between 1.2 and 5; ion temperature and normalised potential are adjusted to keep the peak energy and full width at half-maximum constant according to Section 4.1 and shown in plot b). The key parameters of the system may be varied by an order of magnitude while the form of the spectrum produced remains virtually unchanged.

| Facility | $M$ | $T$ | $\tilde{\phi}_{\mathrm{max}}$ |
|---|---|---|---|
| UCLA | 1.38 | 483 | 415 |
| Vulcan | 1.43 | 754 | 732 |
| Orion | 1.44 | 821 | 821 |
| TITAN | 1.41 | 824 | 762 |
| LMJ-PETAL | 1.42 | 964 | 905 |

Figure 7: The predictions made by Savin [10] for several different facilities. In that work, $T$ is the electron-ion temperature ratio $\beta_i/\beta_e$ and $\tilde{\phi}_{\mathrm{max}}$ the normalised shock potential which is equivalent to $\beta_i$. These sets of parameters, along with the parameter range compatible with the results of this experiment, are shown in Figure 8

https://royalsocietypublishing.org/doi/
10.1098/rsta.2020.0039.

[7] Snavely, R. A. Intense High-Energy Proton Beams from Petawatt-Laser Irradiation of Solids. *Physical Review Letters* **85**, 2945–2948 (2000).

[8] Cairns, R. A., Bingham, R., Norreys, P. & Trines, R. Laminar shocks in high power laser plasma interactions. *Physics of Plasmas* **21**, 022112 (2014).

[9] Cairns, R. A., Bingham, R., Trines, R. G. M. & Norreys, P. Weak collisionless shocks in laser-plasmas. *Plasma Physics and Controlled Fusion* **57**, 044008 (2015).

[10] Savin, A. *Modelling laser-plasma interactions for the next generation of high-power laser experiments.* Ph.D. thesis, University of Oxford (2019).
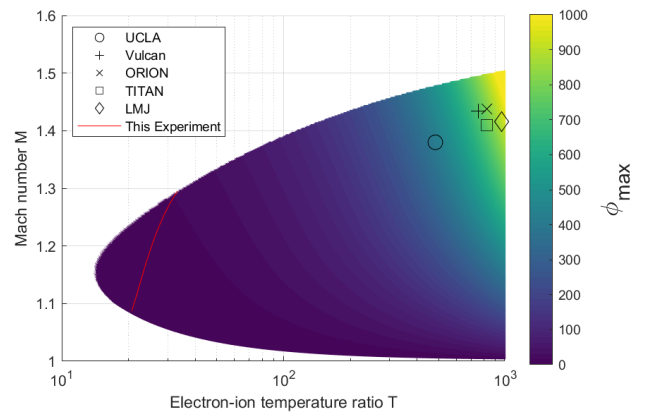
Figure 8: The contents of Table 7, along with the approximate parameter range compatible with the present experiment, plotted on the parameter space shown in Figure 3. The $T$-axis has been scaled logarithmically to improve visibility of the different parameter ranges.

8

[11] Stockem, A., Boella, E., Fiuza, F. & Silva, L. O. Relativistic generalization of formation and ion-reflection conditions in electrostatic shocks. *Physical Review E* **87**, 043116 (2013). URL `https://link.aps.org/doi/10.1103/PhysRevE.87.043116`. Publisher: American Physical Society.

[12] Patankar, S. *et al.* Multiwavelength interferometry system for the Orion laser facility. *Applied Optics* **54**, 10592–10598 (2015). URL `https://www.osapublishing.org/ao/abstract.cfm?uri=ao-54-36-10592`. Publisher: Optical Society of America.

[13] Froula, D. H. *et al.* Optical diagnostic suite (schlieren, interferometry, and grid image refractometry) on OMEGA EP using a 10-ps, 263-nm probe beam **83**, 10E523. URL `https://aip.scitation.org/doi/10.1063/1.4733739`.